Frontiers in Health Informatics
ISSN-Online: 2676-7104
www.healthinformaticsjournal.com
2024; Vol 13: Issue 3
Open Access

Microwave Bone Imaging: Simulation and Experimental Study using Monopole Antenna

[*1]K. Ganapriya, [2]A. Poobalan, [3]K. Kalaivani, [4]Dr .M.Jeyalakshmi

[*1]Assistant Professor/ECE, SSM Institute of Engineering and Technology, Dindigul, India
[2]Assistant Professor/ CSE, University College of Engineering, Dindigul, India
[3]Associate Professor/IT, Vignana Bharathi Institute of Technology, Hyderabad, Telangana. India
[4]Associate Professor /ECE, SSM Institute of Engineering and Technology, Dindigul, India
[*1]ganapriyag@gmail.com, [2]apoobal@gmail.com, [3]kalaivani.sai21@gmail.com, [4]jeyaecessm@gmail.com

Cite this paper as: K. Ganapriya, A. Poobalan, K. Kalaivani, Dr .M.Jeyalakshmi (2024) Microwave Bone Imaging: Simulation and Experimental Study using Monopole Antenna. *Frontiers in Health Informatics, 13* (3), 11199-11212

Abstract

This article looks into the ability of microwave imaging (MWI) to identify fractures in superficial bones, such as the tibia, in a simple and easy arrangement. This approach can be used by first responders to establish a rapid first diagnosis in emergency settings when x-rays are unavailable. It might also be beneficial in cases when x-rays are not suggested (for example, pregnant women or toddlers). In this study, the patch antenna was built to work at frequencies ranging from 1 to 3 GHz. The sensor detects fracture depths of 0.2, 0.5, 1 and 2 mm. The results were compared to the antenna's S-parameters measured in free space and in bone with no fractures. Initially, the dielectric characteristics of human heel tissue were investigated. Next, the suggested approach scans a bone model with simulated fractures using a 2.4 GHz monopole antenna. Skin and background artifacts were removed using a singular value decomposition (SVD) approach, and the findings were compared to S-antenna parameters measured in free space and on unfractured bone. The S-parameter results show how well microwave sensor technology works as a less expensive substitute for human fracture detection. Ex vivo animal bones and multilayer phantoms were used in a number of full-wave studies and simulations to verify this technique. The findings demonstrated that, even in the presence of two millimeters of skin covering a transverse fracture, the system could identify and localize fractures as tiny as 1 mm broad and 13 mm deep.

Keywords: microwave imaging (MWI), x-rays, patch antenna, singular value decomposition (SVD), unfractured bone.

Introduction

Bones play a vital role in the human body, providing the structure needed for movement and supporting our shape. It performs essential functions such as storing minerals and providing mechanical strength to soft tissues and organs [1,2]. Despite their light composition, bones are strong enough to support the entire body mass. Fractures can occur for several reasons, including osteoporosis, which is often associated with a vitamin D deficiency and leads to increased bone fragility. Accidents often result in bone fractures and, in the most serious cases, death. The tibia, or tibia, is the longest bone in the lower leg and is particularly susceptible to fractures. Tibial fractures are common in children, athletes, and the elderly, making initial diagnosis difficult [3].

Magnetic resonance imaging (MRI), computed tomography (CT), and X-rays are crucial diagnostic instruments

for assessing bone disorders, such as fractures and joint issues. Every technique has its limitations, though. Since X-rays are the most rapid and straightforward method of detecting fractures, they are often used. However, they expose people to radiation, pose a risk to public health, particularly for expectant mothers and newborns, and offer scant knowledge about the muscles, tendons, and joints [4,5].

CT scans are a particularly useful tool for obtaining finely detailed pictures of minor abnormalities and complicated fractures. They are limited in usage, nevertheless, because they also subject patients to ionizing radiation. When X-rays do not offer adequate information, CT and MRI are frequently advised; nevertheless, MRI is more costly and time-consuming. According to World Health Organization (WHO) standards, extended exposure to radiation increases the risk of cancer [6,7].

Children and the elderly are more vulnerable to fractures from falls. 15% of all fractures in children are tibial fractures, which rank third among long bone fractures. Non-ionizing and non-invasive screening techniques would be highly helpful given the high frequency of superficial bone fractures. Because microwave imaging is safe and effective for imaging human organs, it remains a popular diagnostic choice despite advancements in other imaging technologies. The technique may be used to monitor and detect a range of illnesses since it utilizes the changes in microwave frequencies between healthy and sick tissue [8,9,10].

Non-intrusive microwave testing facilitates quicker and more straightforward problem discovery in a variety of industries, including electronics. Planar microwave sensors have garnered significant attention lately as a non-destructive testing method. Without being observed, these sensors are able to find flaws located deep beneath the surface [11,12]. In the past, testing were conducted using large waveguide arrays; open rectangular waveguides and horn antennas were commonly utilized to identify material defects. Over the last decade, microwave sensors integrating printed transmission lines and patch antennas have been utilized to monitor and analyze the dielectric characteristics of materials [13, 14, 15].

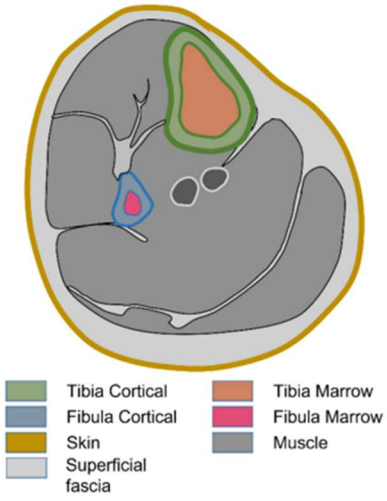

FIGURE 1:Cross-Sectional Anatomy of the leg

The progress given in this study is based on an earlier preliminary evaluation of this technique by the authors, which was based on simulations in [16, 17] and experimental findings in [18]. As far as the authors are aware, no other book concurrently tackles the difficulties in identifying minor transverse fractures, the constraints of non-contact pneumatic systems appropriate for real-world uses, and showcases their efficacy through the use of actual biological bones.

Literature Survey

Microwave imaging (MWI) relies heavily on the dielectric difference between target anatomical tissues to reconstruct dielectric characteristics. Furthermore, the MWI device's operational frequency range primarily determines the spatial resolution of the reconstructed picture and the maximal penetration of the electromagnetic field into the target tissue. The goal of this work is to solve these constraints before developing MWI devices for osteoporosis management. First, we investigated the human heel tissue's dielectric characteristics.

To find the ideal frequency range and matching medium, we then take the transmission line (TL) form. Next, we model the human heel mathematically. We examine power loss, received signal intensity, and electric field penetration in a five-layer bead model using FDTD simulations. Initial findings from CST simulations on electric field penetration validate the use of the TL shape for frequency band selection [18]. The dielectric contrast of the target anatomical region and the TL formalism approach might be useful tools when constructing the MWI system, as this early feasibility analysis shows.

These results support the idea of using MWI sensors to track bone health. The goal of future study is to test a MWI prototype on a bone model before developing it for use in bone imaging. The MWT method will be utilized to rebuild the dielectric characteristics of these models. The creation of a MWI tool to measure the dielectric characteristics of bone in vivo will aid in the monitoring of bone quality and offer a low-cost, portable, non-invasive method of evaluating bone health [19].

[20] examined fracture detection at different depths using microwave imaging technology. Changes in S-parameters (amplitude versus frequency) in the frequency range from 3.5 to 8.5 GHz were recorded in free space and when merged with bone models without fractures and with fracture sizes of 1 mm, 2 mm and 2 mm. 5 mm The results show that the free space configuration produces the best frequency amplitude and bandwidth, while a slot depth of 5 mm shows the lowest amplitude and bandwidth. These results confirm that microwave sensors can be used effectively for medical imaging and diagnosis of human fractures, as well as distinguishing the extent or depth of fractures, providing information on the healing process [21].

In superficial bones like the tibia, tiny, arbitrarily oriented fractures may be detected with a portable, small, low-complexity, non-contact microwave imaging (MWI) equipment, as this work shows. Since our earlier inverse scattering formulation was based on 2D measurement data from a single line scan, this development involves generalizing it to accommodate 3D geometries. Furthermore, research has progressed from testing on dismantled bones or idealized cylinder models to thorough assessments of complete sheep and goat legs, including all related natural tissues like skin and hair. By enhancing fracture localization and identification, cylindrical grid scanning offers important insights into the shape and depth of fractures [22].

We achieved signal-to-noise ratio (SCR) quality metric levels even with complete tissue preservation, without requiring prior knowledge of the phantom shape, and without imposing strict requirements in the legs. Our image reconstruction system effectively recognized all tested fractures placement restrictions. We evaluate the resolution of the system and find that it is close to the theoretical limit [23]. Furthermore, we demonstrate that the method is robust to uncertainties in estimates of dielectric constant and tissue thickness, as well as slight involuntary patient movements during the examination, which are common in clinical settings.

Methodology

DIELECTRIC CHARACTERISTICS

As seen in Figure 2, which is taken from the 20th American edition of Gray's Human Anatomy, the leg is made up of a heterogeneous variety of tissues, including bones, muscles, tendons, veins, arteries, and nerves. The tibia and fibula are the two primary bones of the leg.

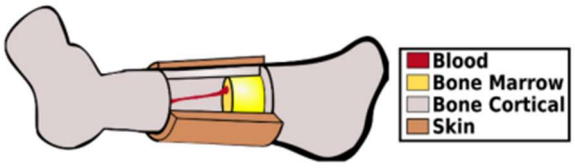

FIGURE 2: Schematic illustration of a tibia bone segment.

The medial side of the tibia is shown to be subcutaneous and devoid of muscle covering, which enhances the higher frequency microwave penetration and may increase the resolution in identifying tiny fractures. Prior to applying the suggested microwave imaging method to actual biological models, simplified skeletal representations were utilized for numerical and experimental simulations.

In order to integrate the dielectric characteristics of the cortical bone and depict the tibia, a uniform cylindrical shape was first constructed. Without getting bogged down with geometry, this first stage is crucial to understanding fracture detection and identifying critical elements that may impede fracture diagnosis. In the portions that followed, the model was further improved to more closely resemble the actual skeleton's shape and composition, incorporating actual biological bones for the experimental assessment. The streamlined material layers utilized in the in vitro sample's numerical model are depicted in Figure 2.

Since medullary bone is the outermost layer, it is regarded as a single homogeneous medium with the same dielectric characteristics (ε, σ) as cortical bone for image reconstruction purposes. Since we were concentrating on the outermost portion of the tibia, muscle tissue was not included in the model. The bone tissue in our model is covered in a layer of skin. When a fracture occurs, multiple tiny internal blood arteries are damaged, causing the fracture to fill with blood. Both models and numerical models adequately capture this characteristic. These materials' complicated permittivity is well-documented. Notably, age-related variations in water content can cause variations in the dielectric characteristics of tissues between patients. As will be shown in a moment, the technique proved robust to these changes.

Dielectric properties of mimicking liquid mixtures

The dielectric contrast between the tissues at the target anatomical site plays a major role in the reconstruction of the dielectric characteristics of biological tissues using microwave imaging (MWI). The trabecular bone has to show a noticeable dielectric difference with the human bone other tissues in order to be diagnosed with osteoporosis. The contrast between the skin, fat, muscle, cortical bone, and trabecular bone of the heel was examined in this study. The dielectric characteristics of these fabrics were detailed by Gabriel et al. [15], who covered a frequency range of 0.5 to 5 GHz in their dielectric measurement data. The authors conducted comparable experiments.

Additionally, the epidermal depth of the tissue was examined in order to assess the depth of penetration of the electromagnetic waves as a function of frequency. Gabriel et al. also collected skin depth data. For the same frequency range, [14] showed the skin depth of different biological tissues as a function of frequency. Plotting of the data was done with MATLAB (The MathWorks, Natick, MA, USA). The human bone anatomy and bone structure are seen in Figures 3(a) and 3(b), respectively.

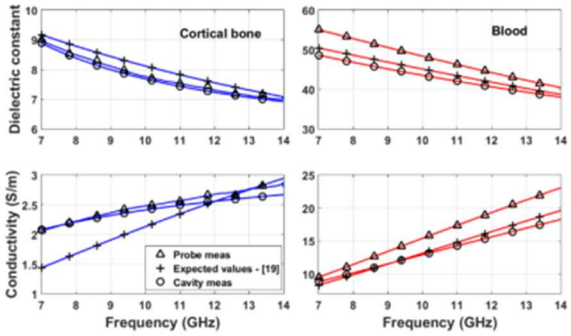

FIGURE 3: Dielectric characteristics of the synthetic mixes that resemble human cortical bone (blue lines) and blood (red lines). The predicted values for biological tissues are shown by crosses [19].

Antenna Design for Microwave Imaging System

In this study, a microwave sensor for medical diagnosis is proposed, focusing on the detection of human fractures. For higher resolution images, shorter wavelengths are preferred, in line with standard requirements for medical imaging equipment. Obtaining these high-resolution images requires the selection of antennas with wide bandwidth, compact dimensions, and directional radiation patterns operating in near-field mode [4]. However, higher frequencies typically result in reduced penetration depth. In this study, the frequency range of 1-3 GHz was chosen for the designed sensor. Metamaterials are used to minimize the overall size of the antenna. This design measures 18.5mm x 11mm x 1mm. Figure 4 below shows the dimensions used in designing an antenna with a microstrip port. All materials used in the antenna design are detailed in Table 1.

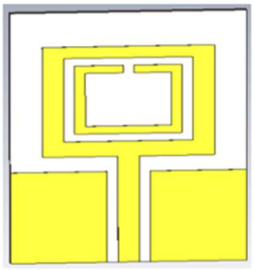

FIGURE 4: An image of the CST-designed monopole antenna illustrating the dimensions utilized in the antenna design.

TABLE 1: Details the components of the antenna design along with the types of materials used for each component.

Component	Material Type
Substrate	FR-4 (lossy)
Patch	Copper (annealed)

Phantom descriptions and Propogation

Three-layered models of two bone lesions were created. These layers mimic the following: i) the medullary layer (internal layer); ii) the cortical bone (outer layer); As seen in Figure 5(a), the lesion in the first model, which depicts a fracture, is situated between the outer and inner layers. The lesion in the second model (Fig.

5(b)) lies inside the inner layer and depicts a lesion in the bone marrow. The various bone layers were replicated using specialized fluids from ZMT Zurich Medical Technologies [11]. The exterior layer, which resembles cortical bone, is represented by TLe11.5C.045 liquid oil, while the interior layer, which resembles bone marrow, is comprised of Tle5C24 liquid oil.

A 40% glycerol and 60% water combination was used to mimic the lesions [12]. TLe11.5C.045, Tle5C24, and the glycerol-water combination have the following dielectric constant and conductivity values: εr = 7 and σ = 0.3 S/m; εr = 5 and σ = 0.2 S/m; and σ = 2 S/m, respectively. It is noteworthy that these conductivity and permittivity values, which were obtained at 2 GHz, may be regarded as typical values for composite lesions of the blood, bone marrow, and cortical bone [9].

Materials to simulate cortical bone and bone marrow were placed in two cylindrical plastic containers with diameters of 11 cm and 7 cm, respectively. The inclusions were kept contained in a 4 mm-diameter cylindrical tube (see Figure 5). In particular, Figure 6(a) illustrates the placement of the bone marrow damage model, and Figure 6(b) illustrates the fracture injury model.

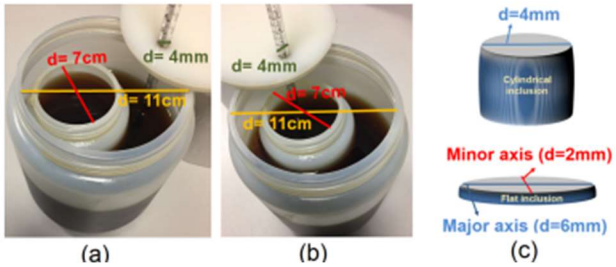

FIGURE 5: Constructed phantoms for (a) bone break, (b) bone marrow bleed, and (c) cylindrical inclusion cross-section in comparison to flat inclusion.

FIGURE 6: Schematic view of bone marrow (a), and bone fracture lesion (b).

Imaging procedure

An imaging algorithm based on the Huygens principle [14] is used to the observed complex S21 values in order to produce pictures. The received signal can be expressed as S21np,m(a0, φnp; txm; f), where np = 1, 2,…, 80, m = 1, 2,…, 10, f represents the frequency, assuming that the receiver (rx) can be rotated to capture the received signal at points defined as rxnp == (a0, φnp) == −→ρ np moved along a circular surface of radius a0. To eliminate artifacts, a rotational subtraction technique is used, utilizing equation (1). The process involves deducting the signal that is acquired from the emission positions m and m+1, which are part of the same doublet, from each other.

$$E_{HP,2D}^{testr}(\rho,\phi;tx_m - tx_{m+1};f)$$
$$\propto \Delta s \sum_{np=1}^{N_{PT}} \left(\left(S21_{np,tx_m}^{known} - S21_{np,tx_{m+1}}^{known} \right) G\left(k_1 \left| \overrightarrow{\rho n_p} - \overrightarrow{\rho} \right| \right) \right) \quad (1)$$

The observation point is denoted by (ρ, φ) ≡ −→ρ in the formula, the spatial sampling interval is denoted by Δs, and the number of receiving points is indicated by NP T. The wavenumber is denoted by the k1 component, while the Green's function is represented by G. The "rcstr" label represents the "reconstructed" internal field, while the HP label denotes the employment of the Huygens-based procedure in equation (1). Further information is available in [14] and [15]. The total of several pictures, each derived from the incoherent sum of all frequency components and corresponding to distinct emission doublets, determines the final image's intensity. Consequently, the following formula is used to create a composite picture of the five emission position doublets (where NF stands for the number of frequency samples):

$$I(\rho,\phi) = \sum_{m=1}^{S} I(\rho,\phi; tx_{2m-1} - tx_{2m})$$

$$= \sum_{m=1}^{5} \sum_{i=1}^{N_F} \left| E_{HP,2D}^{restr}(\rho,\phi; tx_{2m-1} - tx_{2m}; f_i) \right|^2 \qquad (2)$$

Imaging quantification

Two measures (i) resolution and (ii) signal-to-cluster ratio (S/C) are presented and computed to assess the algorithm's detection capacity. Resolution is specifically defined as the area in which the normalized intensity is greater than 0.5 [15]. The greatest intensity recorded inside the lesion region divided by the maximum intensity outside the lesion area is the definition of the S/C ratio [16].

Signal Processing in Frequency Domain

This study aimed to determine the depth of human bone fractures by analyzing changes in the dielectric properties of the surrounding tissue. To characterize these tissues, a monostatic radar setup was used in our microwave detection system. The antenna's reflection coefficient is measured in free space to evaluate its efficiency, and the electric field strength is used to determine the most responsive area of the antenna. This information helps predict the location and the optimal direction of the antenna. Move the antenna over the surface of the body to be studied. The S-parameters are frequency dependent and are therefore suitable for analyzing the processed signal in the frequency domain. Therefore, the following equation uses the parameter S which represents the reflection coefficient of a single port network.

$$Z_{in} = Z_0 \left(\frac{1+S_{11}}{1-S_{11}} \right) \qquad (3)$$

Results and discussion,

Dielectric properties contrast of tissues present in the human bone

The dielectric characteristics of each heel tissue are shown in Figure 9. 0.5 to 5 GHz is the frequency range. The dielectric distribution reveals notable variations in the relative permittivity and conductivity among the many tissues present in the bead. Specifically, as Figure 7 illustrates, trabecular bone has dielectric characteristics that are notably different from those of the surrounding tissue. Between skin and trabecular bone, the mean percentage variations in relative permittivity and conductivity were 70% and 56%, respectively. Similarly, the average percentage variances between cortical and trabecular bone were 65% and 48%, respectively, in the 0.5 to 5 GHz range. The use of microwave imaging (MWI) to distinguish and reconstruct the heel tissues is supported by the notable dielectric difference between the dielectric properties of trabecular bone.

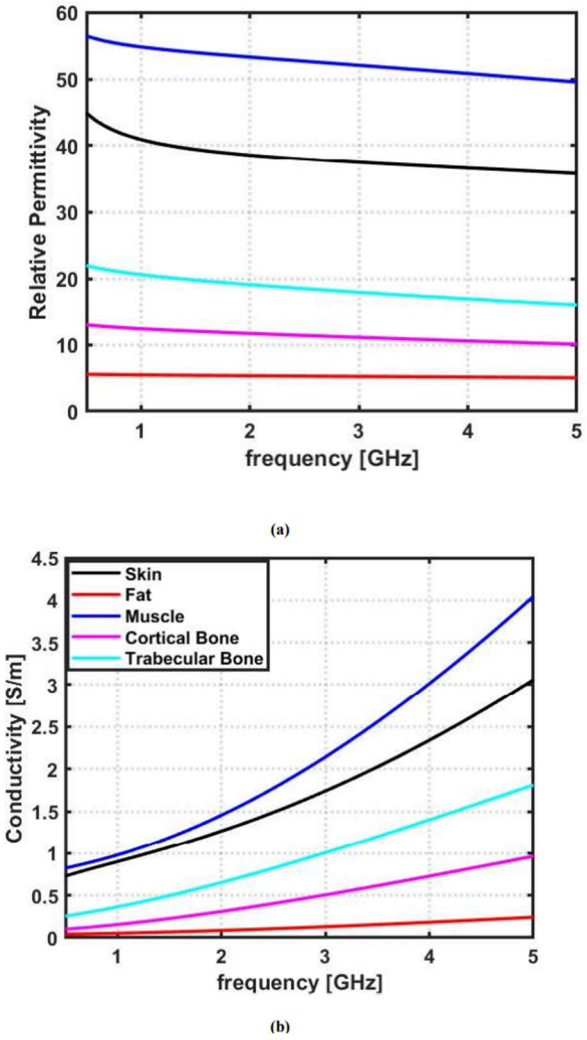

FIGURE 7: Dielectric properties of the tissues in human bone: (a) Relative Permittivity; (b) Conductivity

FRACTURE DETECTION AND IMAGING PERFORMANCE

Figure 8 displays the general geometry of the reference scenario. The primary bone was designed as a homogeneous cylindrical object with expanded parts at both ends, measuring 80 mm in length and 19 mm in diameter. A homogeneous cylinder of 100 mm in length and 7.6 mm in diameter, with a gap of 7.6 mm between the margins of the two cylinders, represents the neighboring bone. The distance between the margins of the tibia and fibula is based on [14], and the ratio between their diameters at the middle is based on [39]. The dielectric characteristics of cortical bone are shared by both forms. A half-disc model filled with blood, measuring 1 mm in thickness and 13 mm in depth, was used to illustrate the fracture.

TABLE 2: Average permittivity used for the biological tissues

Tissue	ε_r	$tan\delta$
Cortical bone	8	0.58 (mixture)
Blood	49	0.58 (mixture)

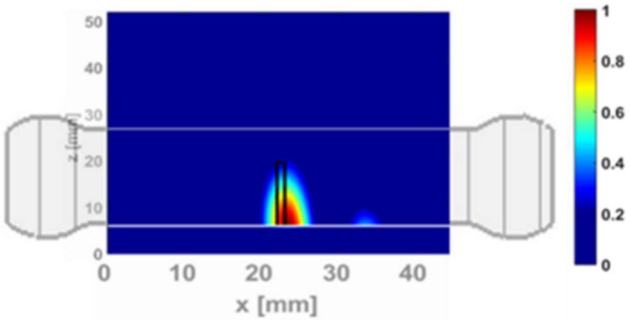

FIGURE 8: Reconstructed image of cylindrical phantom representing the fractured tibila ($z_{Bone} = 6mm$), and fracture located 22 mm ≤ x_{Bone} ≤ 23 mm filled with blood (1 mm), in a planar section. The black dotted contour identifies the fracture region. The antenna scans at 0 mm ≤ x_j ≤ 44 mm, z=0.

EXPERIMENTAL RESULTS

One of the measurement configurations in our lab is shown in Figure 9. It is made up of a polystyrene platform that holds the creature's model or skeleton in place.

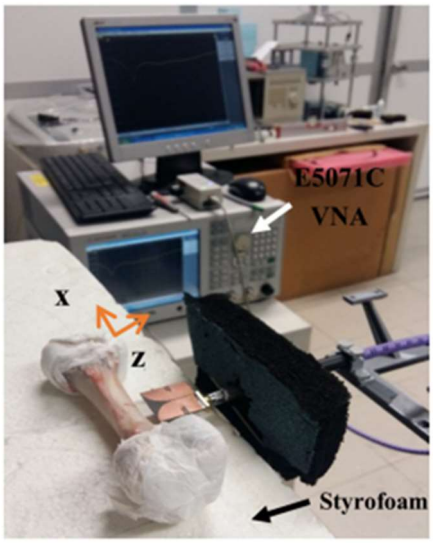

FIGURE 9: Details of the configuration of one of the microwave imaging systems.

Figure 10 shows the bandwidth of the designed and tested antenna in the frequency range of 1 to 3 GHz. This

shows that the antenna can operate effectively in a wider bandwidth, as demonstrated by the -10 dB threshold shown in the figure. At this -10 dB level, the antenna reaches its maximum bandwidth when tested in free space and is not affected by any body tissue that may interfere with radiation propagation due to its dielectric properties.

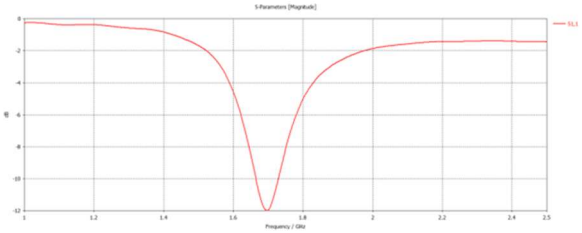

FIGURE 10: A Graph of S-Parameter depicting the actual bandwidth of the antenna when tested in free space

The S-parameters shown in Figures 11 were recorded during the antenna test in the frequency range from 3.5 to 8.5 GHz. The graph shows a significant deviation from the results in Figure 14, where the same antenna was tested in free space. This indicates reduced voltage flow or propagation across the port input impedance, resulting in lower amplitudes than those observed with antennas tested in free space.

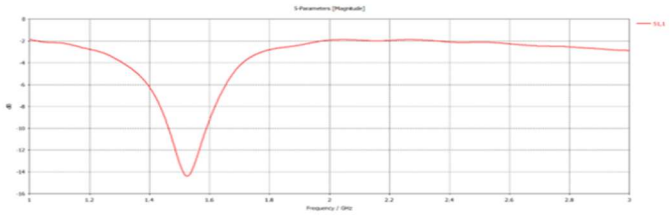

FIGURE 11: A Graph of S-Parameter depicting the actual bandwidth of the antenna when tested on the bone phantom Without fracture

This difference may be due to the presence of a 1 mm fracture introducing blood into the tissue components of the model. The dielectric properties of the hematoma (blood) in the fracture area cause increased distortion of radiation propagation. Figure 12 depicts as Graph of S-Parameter depicting the actual bandwidth of the antenna when tested the bone phantom with a Fracture.

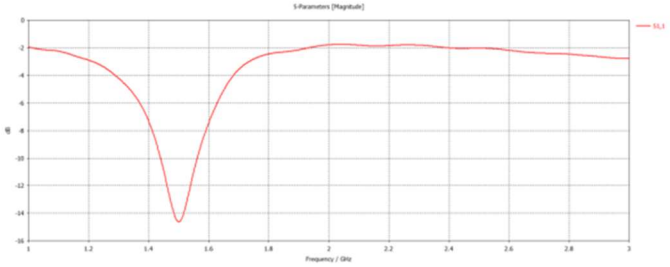

FIGURE 12: A Graph of S-Parameter depicting the actual bandwidth of the antenna when tested the bone phantom with a Fracture Depth of 2mm.

Table 4 depicts as State of the art comparison.

TABLE 3: Comparison of the state of the art on bone microwave imaging with our work

REF	MEDIUM	OBJECTIVE	PHANTOM	CONFIGURATION	COMMENT
[9]	Contact with the body patient	Reconstruction of bone profiles	Regular boundary tubes using a manufactured phantom with animal tissues (tibia, fibula, muscle and fat)	Two antennas are used in the scan (s11 and s21 responses)	Requires coupling medium Does not address fracture
[10]	Free space Contactless with the body patient	Detecting longitudinal bone fracture and lesions	Regular boundary tubes representing the cortical bone, bone marrow and a lesion; Longitudinal lesion (radius of 3 mm and Extension of 130 mm)	Two antennas are used in the scan (s11 and s21 responses)	Fractures are quite large The system is bulky and expensive
[11]	Free space Contact with the body patient	Detecting transversal bone fracture of about 1 mm	Realistic phantom composed of human tibia, muscle, fat and porcine skin with irregular boundary	User a planar sensor in contact with the patients skin (s11 and s21 responses)	Unrealistic precision is required for antenna contact with the body
Our Work	Free space Contactless with the body patient	Detecting transversal bone fracture of about 1 mm	Realistic phantom composed of animal tibia and skin with irregular boundary	A single antenna is used in radar mode (s11 response)	

CONCLUSION

This paper offers a microwave imaging approach for detecting and localizing superficial transverse bone fractures utilizing a simple setup that avoids the requirement for liquid immersion and employs only one scanning antenna. The absence of touch with the liquid creates issues for the removal of skin artifacts, which may be overcome using specific algorithms. These algorithms can also deal with bone and skin heterogeneities. The approach was verified using simulations and tests on bone models, as well as ex vivo animal bones and skin. The findings indicate that fractures up to 1 mm thick may be diagnosed and located despite changes in bone borders and extra layers. The dielectric characteristics of phantom or animal bones differ from those utilized in the inversion technique, however this has no effect on fracture diagnosis or localization. This proposed arrangement lends itself nicely to being turned into a working device for therapeutic purposes. These findings lend support to the development of a portable device for more extensive biological sampling of the extremities.

References

[1] Parvathala, Balakesava & Manikandan, A. & Vijayalakshmi, P. & Parvez, M. & Gopalan, S. & Ramalingam, S.. (2024). Bio-Inspired Metaheuristic Algorithm for Network Intrusion Detection System of Architecture. 10.4018/979-8-3693-5276-2.ch004

[2] Ali, R., Manikandan, A., Lei, R. et al. A novel SpaSA based hyper-parameter optimized FCEDN with adaptive CNN classification for skin cancer detection. Sci Rep 14, 9336 (2024). https://doi.org/10.1038/s41598-024-57393-4.

[3] Kolli, Srinivas & V., Praveen & John, Ashok & Manikandan, A.. (2023). Internet of Things for Pervasive and Personalized Healthcare: Architecture, Technologies, Components, Applications, and Prototype Development. 10.4018/978-1-6684-8913-0.ch008.

[4] Palaniappan, Mathiyalagan & Annamalai, Manikandan. (2019). Advances in Signal and Image Processing in Biomedical Applications. 10.5772/intechopen.88759.

[5] V. A.R, S. David, E. Govinda, K. Ganapriya, R. Dhanapal and A. Manikandan, "An Automatic Brain Tumors Detection and Classification Using Deep Convolutional Neural Network with VGG-19," *2023 2nd International Conference on Advancements in Electrical, Electronics, Communication, Computing and Automation (ICAECA)*, Coimbatore, India, 2023, pp. 1-5, doi: 10.1109/ICAECA56562.2023.10200949.

[6] Ali, R., Manikandan, A. & Xu, J. A Novel framework of Adaptive fuzzy-GLCM Segmentation and Fuzzy with Capsules Network (F-CapsNet) Classification. *Neural Comput & Applic* (2023). https://doi.org/10.1007/s00521-023-08666-y

[7] Dr.S. Vijayalakshmi. Early detection of breast cancer using robust back propagation neural network classifier. Rom Biotechnol Lett. 2022; 27(2): 3407-3415 DOI: 10.25083/rbl/27.2/3407.3415

[8] S. Sadesh, Dinesh Valluru**.** A. Manikandan. Hybrid Approach for Human Diseases Prediction Using Air Quality Index. Rom Biotechnol Lett. 2022; 27(1): 3270-3281 DOI: 10.25083/rbl/27.1/3270-3281

[9] Annamalai, Manikandan & Muthiah, Ponni. (2022). An Early Prediction of Tumor in Heart by Cardiac Masses Classification in Echocardiogram Images Using Robust Back Propagation Neural Network Classifier. Brazilian Archives of Biology and Technology. 65. 10.1590/1678-4324-2022210316.

[10] Manikandan, Annamalai, M,Ponni Bala. (2023). Intracardiac Mass Detection and Classification Using Double Convolutional Neural Network Classifier. Journal of Engineering Research. 11(2A). 272-280. 10. 36909/jer.12237.

[11] Balamurugan, D. & Seshadri, s.Aravinth & Reddy, P. & Rupani, Ajay & Manikandan, A.. (2022). Multiview Objects Recognition Using Deep Learning-Based Wrap-CNN with Voting Scheme. Neural Processing Letters. 54. 1-27. 10.1007/s11063-021-10679-4.

[12] Bommaraju, K., Manikandan, A., & Ramalingam, S. (2017). Aided System for Visually Impaired People in Bus Transport using Intel Galileo Gen-2: Technical Note. *International Journal of Vehicle Structures and Systems*, *9*(2), 110–112. https://doi.org/10.4273/ijvss.9.2.09

[13] Manikandan, A., Ramalingam, S., & Aathi bhagavan, V. (2016). Potholes Alert System for Riders. *International Journal of Advances in Natural and Applied Sciences*, *10*(9), 440–444.

[14] Amit Grover, A. Manikandan, Vivek Soi, Anu Sheetal, Mehtab Singh, Realisation of white LED using fiber based hybrid photonic structures, Optoelectronics and Advanced Materials - Rapid Communications, 15, 11-12, November-December 2021, pp.521-527 (2021).

[15] Manikandan, A., & Nirmala, V. (2015). A Low Cost Thermoelectric Refrigerator. International Journal of Applied Engineering Research, 10(55), 3097–3101

[16] Sheikdavood K, Surendar P, Manikandan A. Certain Investigation on Latent Fingerprint Improvement through Multi-Scale Patch Based Sparse Representation. Indian Journal of Engineering. 2016; 13(31):59-64.

[17] Yago Ruiz, Á., Cavagnaro, M. & Crocco, L. An effective framework for deep-learning-enhanced quantitative microwave imaging and its potential for medical applications. Sensors 23, 643 (2023).

[18] Janjic, A., Akduman, I., Cayoren, M., Bugdayci, O. & Aribal, M. E. Safe-microwave imaging device for breast cancer early screening and diagnostics. In Electromagnetic Imaging for a Novel Generation of Medical Devices: Fundamental Issues, Methodological Challenges and Practical Implementation, 273–292 (Springer, 2023).

[19] Song, J., Shen, T. & Wang, Q. An image post-processing approach based on fully dense u-net for microwave induced thermo-acoustic tomography. IEEE J. Electromagn. RF Microwaves Med. Biol. 7, 59–64 (2022).

[20] Saraswat, D. et al. Explainable ai for healthcare 5.0: opportunities and challenges. IEEE Access 10, 84486–84517 (2022).

[21] Shukla, P. K. et al. Ai-driven novel approach for liver cancer screening and prediction using cascaded fully convolutional neural network. J. Healthc. Eng. 2022, 4277436 (2022).

[22] Shukla, P. K. et al. Ai-driven novel approach for liver cancer screening and prediction using cascaded fully convolutional neural network. J. Healthc. Eng. 2022, 4277436 (2022).

[23] Mello-Thoms, C. & Mello, C. A. Clinical applications of artificial intelligence in radiology. Brit. J. Radiol. 96, 20221031 (2023).